Magnetic Resonance Imaging 119 (2025) 110369

Contents lists available at ScienceDirect

Magnetic Resonance Imaging

journal homepage: www.elsevier.com/locate/mri

MRI as a viable alternative to CT for 3D surgical planning of cavitary bone tumors

Yooseok Chae [a,1], Giles Michael Cheers [a,1,*], MinJoo Kim [a], Paul Reidler [b], Alexander Klein [a], Thomas Fevens [c], Boris Michael Holzapfel [a], Susanne Mayer-Wagner [a,*]

[a] Department of Orthopaedics and Trauma Surgery, Musculoskeletal University Center Munich (MUM), Ludwig Maximilian University (LMU) University Hospital, LMU Munich, 81377 Munich, Germany.
[b] Department of Radiology, LMU University Hospital, LMU Munich, 81377 Munich, Germany.
[c] Department of Computer Science and Software Engineering, Concordia University, Montréal, Canada

ARTICLE INFO

Keywords:
Segmentation
Bone defects
CT
MRI
Imaging
Preoperative
Tumors

ABSTRACT

Cavitary bone defects, defined as a volumetric loss of native bone tissue, require accurate preoperative imaging for treatment planning. While CT (computed tomography) has traditionally been the gold standard for segmentation due to its superior resolution of cortical bone, MRI (magnetic resonance imaging) offers unique advantages, particularly in visualizing the soft tissue–bone interface. Furthermore, MRI eliminates the ionizing radiation associated with CT, making it an advantageous alternative, especially in the management of benign and low-grade malignant bone tumors. Despite these advantages, MRI's inherently lower spatial resolution may introduce artifacts, which can complicate segmentation accuracy. This study evaluates the feasibility of MRI as a viable alternative to CT in the preoperative planning of cavitary bone defect treatment. We analyzed CT and MRI scans from 80 patients with benign and locally aggressive primary bone tumors, generating three-dimensional (3D) models through manual segmentation in Mimics, validated using Geomagic Control X. Volumetric differences between the CT- and MRI-derived models were assessed using the Wilcoxon signed-rank test and paired *t*-test. The mean volumetric difference between MRI and CT scans was 2.68 ± 1.44 %, which was not statistically significant ($p = 0.15$). Additionally, multiple regression analysis examining sex, age, and diagnosis revealed no significant differences in the 3D model volumes derived from the two imaging modalities (sex: $p = 0.51$, age: $p = 0.98$, and diagnosis: $p = 0.50$). These results support MRI-based segmentation as a reliable, radiation-free alternative to CT, particularly when precise delineation of soft tissue boundaries is critical for surgical planning.

1. Introduction

Cavitary bone defects, marked by the volumetric depletion of natural bone tissue, arise from diverse pathological conditions, including ABC (aneurysmal bone cyst), GCT (giant cell tumor of bone), enchondroma, ACT (atypical cartilaginous tumor), chondroblastoma, CMF (chondromyxoid fibroma), and osteoblastoma [1–5]. These defects are classified as benign and locally aggressive primary bone tumors, with incidence rates ranging from 5.7 % to 27.7 % of all bone tumors [6]. Although approximately 40 % of musculoskeletal proliferative lesions are benign and non-metastatic [7], they still pose significant clinical risks [8]. These risks encompass the potential for tumor expansion, which can impinge on surrounding healthy tissues, potentially causing fractures or neurological deficits [8,9].

Diagnostic approaches currently employed, such as X-ray, CT (computed tomography), and MRI (magnetic resonance imaging), are crucial for identifying bone tumors [10]. However, accurate diagnosis remains challenging due to the asymptomatic nature of these tumors and the radiological similarities among cavitary bone defects [11]. Treatment strategies are typically determined by the type of primary bone neoplasm, patient symptoms, and the treatment-related morbidity [12]. The classification of tumors by biological behavior, as proposed by Wolf and Enneking [13], further informs treatment planning: non-surgical management is sufficient for latent and asymptomatic lesions, such as fibrous cortical defects or non-ossifying fibromas, though radiological follow-up after 3–6 months is recommended [5]. Conversely, active (e.

* Corresponding authors at: LMU Klinikum Campus Großhadern Marchioninistr. 15, 81377 Munich, Bavaria, Deutschland.
E-mail addresses: giles.cheers@med.uni-muenchen.de (G.M. Cheers), susanne.mayer@med.uni-muenchen.de (S. Mayer-Wagner).
[1] Yooseok Chae and Giles Michael Cheers, contributed equally to this work

https://doi.org/10.1016/j.mri.2025.110369
Received 19 January 2025; Received in revised form 24 February 2025; Accepted 2 March 2025
Available online 4 March 2025

g., CMF, enchondroma) and aggressive (e.g., aggressive ABC, GCT, chondroblastoma, osteoblastoma) bone tumors frequently necessitate surgical interventions, including curettage (the preferred treatment for most benign tumors), RFA (radiofrequency ablation), excision, and reconstruction [5]. Given that even minor diagnostic errors can lead to surgical failure, protracted recovery, or deterioration in the patient's quality of life, technologies that enhance diagnostic accuracy for preoperative planning are of paramount importance.

Medical image segmentation is integral to computer-aided diagnostic systems and surgical planning, enabling precise extraction of critical anatomical features from regions partitioned within the entire image [14]. In contemporary orthopedic surgery, medical image segmentation is crucial for translating diagnostic imaging into actionable surgical plans, as precise preoperative planning directly influences surgical outcomes [15]. To this end, radiological modalities like CT and MRI scans are not only indispensable for diagnosing cavitary bone defects but also serve as the foundation for accurate image segmentation, which facilitates targeted and effective treatment strategies [14,16].

In clinical practice, manually segmented CT images by radiologists or engineers are often regarded as the gold standard due to their precision and reliability, serving as a critical reference for diagnostic and therapeutic decision-making [17]. While advanced methods such as gradient-based techniques (e.g., level-set methods), atlas-based approaches, and deep-learning models (e.g., U-Nets) have been developed and are increasingly utilized for automated segmentation, manual segmentation remains widely employed, particularly in complex cases where automation struggles to achieve the required accuracy. CT imaging operates on the principle of X-ray attenuation, employing a series of X-ray beams from multiple angles to generate cross-sectional images of the anatomy. These images are reconstructed into high-resolution representations of internal structures, quantitatively differentiable based on their respective densities measured by HU (Hounsfield unit) [18]. This capability enables detailed delineation of cortical and trabecular bone structures, making CT particularly effective for bone segmentation and preferred in scenarios requiring high spatial resolution [15,19]. However, threshold-based segmentation of CT scans faces significant challenges, especially in distinguishing between adjacent bone regions that are in close proximity or have similar densities, such as those in the hip or knee joints [20]. This can result in inaccurate segmentation, which may complicate the planning and execution of surgical interventions [20]. Additionally, the ionizing radiation associated with CT is a significant drawback. For instance, it has been reported that the accumulated absorbed dose of radiation, estimated at 50 mSv for individuals under 40 years of age, increases the risk of developing brain tumors, leukemia, and bone fragility [21]. Therefore, minimizing ionizing radiation from CT scans is advantageous for patient care [22].

Unlike CT, which uses X-ray attenuation and HUs to differentiate tissue densities, MRI operates through strong magnetic fields and radio waves to measure tissue relaxation times. These relaxation times vary depending on tissue composition and structure, allowing MRI to generate images with superior soft tissue contrast. Hence, it is the preferred modality for the clinical diagnosis of most cavitary bone defects, such as ABC and GCT [5,12,23]. Furthermore, MRI is particularly advantageous for skeletally immature patients, as it outperforms CT in diagnosing pediatric and juvenile bone structures and, importantly, avoids ionizing radiation. [6,24]. However, MRI provides a lower bone signal due to the lower proton density and slower relaxation times of bone tissue, which presents challenges in bone imaging and can lead to more cumbersome and less accurate manual segmentation. As a result, MRI is less favored for detailed bone analysis compared to CT, despite its advantages in soft tissue visualization and the absence of radiation exposure [25,26].

Given the respective strengths and limitations of CT and MRI in bone imaging, it is important to assess whether these modalities can be used interchangeably in clinical practice. This study hypothesizes that 3D models from CT and MRI scans of cavitary bone defects will show statistically insignificant volumetric differences. If confirmed, this would suggest that CT and MRI could be used interchangeably for preoperative planning depending on clinical needs. By analyzing the volumetric and geometrical differences in segmented CT and MRI scans of various bone tumors, irrespective of their location, we aim to comprehensively evaluate whether MRI can serve as a viable alternative to CT for preoperative planning in the treatment of cavitary bone defects. This evaluation could significantly impact clinical decision-making, primarily for determining the type of defect reconstruction, especially in cases where minimizing radiation exposure is paramount, or where MRI's superior soft-tissue contrast is advantageous.

2. Patient data collection and methods

2.1. Patient selection

To address the aims of this study, we conducted a retrospective analysis using data from 100 patients diagnosed with cavitary bone defects resulting from benign and locally aggressive primary bone tumors. CT and MRI scans were retrieved from the LMU University Hospital patient database. We excluded patients with extraosseous cavitary bone defects or malignant bone tumors with metastasis ($n = 11$), as these aggressive tumors often invade surrounding tissues, leading to distinct findings on MRI scans compared to CT images [27].

To minimize the risk of tumor progression affecting the results, we excluded patients whose MRI and CT scans were taken more than three months apart ($n = 1$), given that most benign bone tumors grow slowly and may not exhibit significant changes within this period [28]. This exclusion was particularly important for aggressive benign tumors, such as GCT, which can show notable growth within this timeframe [29].

Additionally, patients with osteoblastoma were excluded from the study because these lesions are typically subcritical (< 2 cm in diameter) with osteogenic surroundings, and the preferred treatment modality is CT-guided RFA ($n = 2$) [9]. Discrepancies between CT and MRI scans also served as an exclusion criterion ($n = 6$). These discrepancies included cases where lesion sites were obscured, scans with anatomical structures cut off that hindered defect boundaries, and instances where MRI scans had an insufficient number of images to perform meaningful segmentation.

Meanwhile, the number of patients diagnosed with fibrous dysplasia ($n = 3$), non-ossifying fibroma ($n = 1$), unclear osteolysis ($n = 1$), and intraosseous ganglion ($n = 1$) was too small for individual statistical analysis. Therefore, these cases were combined into an unspecified subgroup to streamline and simplify the analysis.

2.2. Data and file formats

CT and MRI scans were extracted as DICOM (digital imaging and communication in medicine) files from the patient database using Visage (v.7.1, Visage Imaging, USA), with all patient information anonymized. Anonymization was further verified using 3D Slicer (v.5.6.1, 3D Slicer Community). The dataset included scans from various machines from different manufacturers, including Siemens, GE Medical Systems, Toshiba, Canon Medical Systems, Curve Beam, PNMS, and Phillips Medical Systems. Scanning protocols also varied as follows: CT voxel sizes ranged from 0.02 to 3.05 mm^3, while MRI voxel sizes ranged from 0.05 to 4.78 mm^3. MRI sequences included T1-weighted, T2-weighted, PD (proton density), and STIR (short tau inversion recovery) sequences. The scans exhibited a T_R (repetition time) of 8 to 6977.66 ms, T_E (echo time) of 2.17 to 2948 ms, NEX (number of excitations) ranging from 1 to 4, frequency bandwidth between 36.68 and 127.76 kHz, flip angles from 10° to 180°, slice thicknesses from 0.64 to 6 mm, pixel sizes between 0.1554 and 1.0313 mm, and image matrices of 190 × 256 to 1024 × 1024.

MRI segmentations were primarily performed on T1-weighted images due to superior contrast for osseous defect delineation. However,

fluid-sensitive sequences (STIR, T2-FS) were used as references to confirm defect boundaries when necessary. The majority of scans were based on 2D sequences, with three CT and two MRI scans acquired using 3D isotropic sequences.

2.3. Segmentation and measurement algorithm

The cavitary bone defects visible in the CT and MRI scans were manually segmented and reconstructed using the biomedical image analysis software Mimics (v.26.0, Materialise, Belgium), and subsequently extracted as 3D models for further analysis, as shown in Fig. 1. Segmentations were performed by a medical doctoral student and subsequently validated on a subsample ($n_{CT+MRI} = 30$) by an experienced engineer, an orthopedic surgeon and a radiologist, with discrepancies resolved by consensus. To assess interobserver agreement (IOA) for volumetric and dimensional measurements, an engineer with experience in musculoskeletal imaging segmented the cavitary bone defects of 30 cases from both CT and MRI datasets. Each observer was blinded to the other's results to prevent bias. Segmentation was performed primarily on axial images, with coronal and sagittal views used for anatomical validation. To ensure consistency and to avoid overestimation from extraosseous tumor components, segmentation was confined exclusively to intraosseous defects. The segmentation process is detailed in Fig. 1.

Initially, global thresholding with HUs using Otsu's method was employed to create a mask of the bone structure. Cavitary defects were then manually segmented using the split mask function, with careful consideration of the surrounding anatomical structures. For MRI scans, thresholding based on HU was not feasible; therefore, the entire scan was selected, and defects were manually segmented using the split mask function. The segmented masks were first converted into STL (binary little-endian mesh) files. Next, the volumes of the 3D models were automatically measured by Mimics and recorded for statistical analysis. Finally, the STL files were used for geometric accuracy assessment.

2.4. Evaluation metrics and 3D model validation

Linear dimensions of the intraosseous defects were determined by extracting the length, width and depth of the 3D model aligned to the axial plane. These linear measurements were obtained from both CT and MRI datasets and serve as primary outcome parameters.

The volumetric differences between the 3D models extracted from CT and MRI scans were assessed by calculating the V_R (relative volume ratio) between V_{CT} (measured volume of the 3D model extracted from CT) and V_{MRI} (measured volume of the 3D model extracted from MRI) using Eq. (1).

$$V_R = \left| \frac{V_{CT} - V_{MRI}}{V_{CT}} \right| \times 100 \quad (1)$$

To validate the accuracy of the segmented 3D models, the geometric surface deviation between the segmented CT and MRI scans was analyzed using Geomagic Control X (v.2020.1, 3D Systems Inc., USA) as illustrated in Fig. 1. MRI models were aligned with the reference CT-derived models through an iterative process, beginning with precise alignment tools, followed by manual adjustments, and concluding with the best-fit alignment using the ICT (iterative closest point) algorithm. After alignment, the meshes were compared geometrically using the 3D Compare module, with automated maximum deviation settings to filter outliers.

2.5. Statistical analysis

Numerical measurement data were compiled in Microsoft Excel (Microsoft Office 2016, Microsoft, USA). Graphs were generated and statistical analysis were performed using GraphPad Prism (version 9.4.0, GraphPad Software Inc., USA). The figures were prepared using Pho-

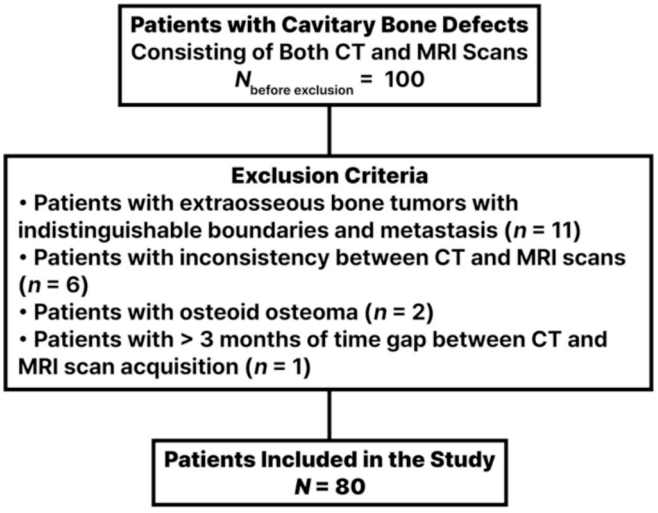

Fig. 2. Flow chart of patient data collection including the exclusion criteria.

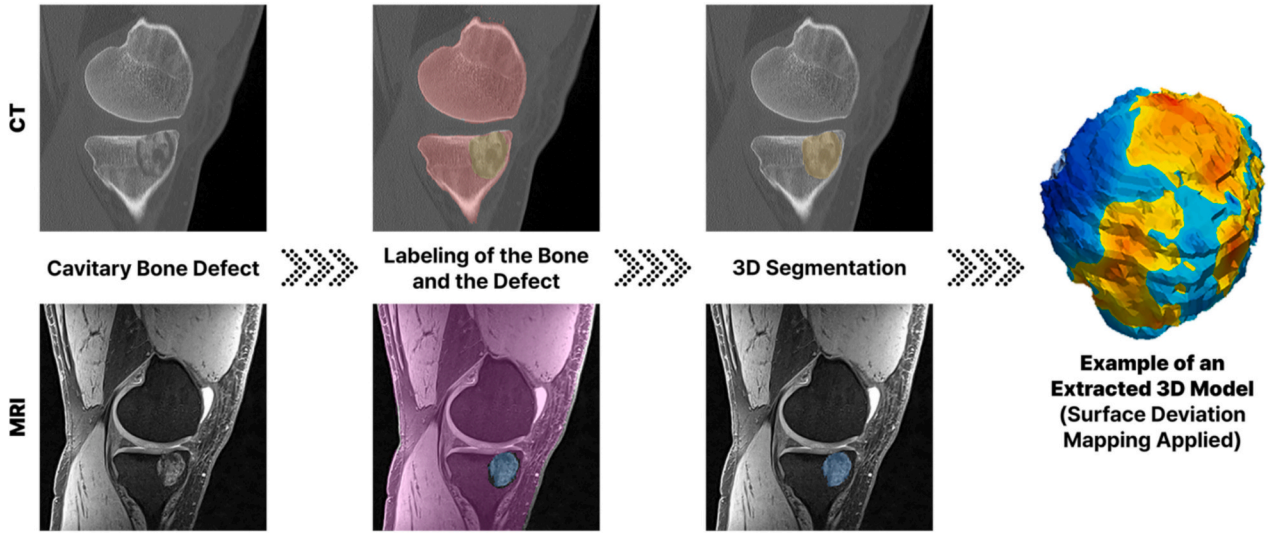

Fig. 1. Schematic overview on the 3D segmentation process of CT and MRI scans and an example of the extracted 3D model of the cavitary bone defect.

toshop (26.0.0 Release, Adobe Inc., USA). The normality of the quantitative data was assessed using the Shapiro-Wilk test. Normally distributed continuous parameters were presented as mean ± SD (standard deviation), while non-normally distributed data were reported as median with IQR (interquartile range). Statistical significance was evaluated using the paired *t*-test for normally distributed data and the Wilcoxon signed-rank test for non-normal data. Multiple linear regression was conducted to assess the effects of sex, age, diagnosis on the volume ratios of the 3D models derived from CT and MRI scans. A 95 % CI (confidence interval) ($\alpha = 0.05$) was applied to all analyses. Interclass and interobserver variability was evaluated using intraclass correlation coefficients (ICCs) for absolute agreement in volumetric and linear (X, Y, Z) dimensions. The ICCs were interpreted using standard benchmarks: <0.50 (poor), 0.50–0.75 (moderate), 0.75–0.90 (good), and > 0.90 (excellent). Further, Bland-Altman plots were used to assess bias and limits of agreement between observers.

3. Results

3.1. Patient data

After applying the exclusion criteria, 80 patient data were included in the study for analysis, as illustrated in Fig. 2. A demographic and clinical characteristics summary of the patient cohort is provided in Table 1. Among the 80 patients, benign bone tumors were observed more frequent in male patients ($n = 47$) than in female patients ($n = 33$), young patients under 20 years ($n = 26$) and those diagnosed with ABC ($n = 23$) and GCT ($n = 24$). The individual demographic and clinical characteristics of the patient cohort are shown in Table 2.

Table 1
Summary of the demographic and clinical characteristics, along with the V_R between V_{CT} and V_{MRI}. V_R: volume ratio; V_{CT}: measured volume of the 3D model extracted from CT; V_{MRI}: measured volume of the 3D model extracted from MRI; IQR: interquartile range; SD: standard deviation; ABC: aneurysmal bone cyst; GCT: giant cell tumor; ACT: atypical cartilaginous tumor; CMF: chondromyxoid fibroma; N/A: not applicable.

Characteristics	Population	Mean ± SD of V_R	Median (IQR) of V_R	*p*-value
CT and MRI				
	N = 80 (100 %)	2.68 ± 1.44 %	2.56 (2.42 %)	0.14
Subgroup: Sex				
Male	*n* = 47 (58.75 %)	2.76 ± 1.40 %	2.84 (2.24 %)	0.18
Female	*n* = 33 (41.25 %)	2.58 ± 1.50 %	2.49 (2.20 %)	0.43
Subgroup: Age				
0–19 Years	*n* = 26 (32.50 %)	2.76 ± 1.54 %	3.01 (2.78 %)	0.12
20–39 Years	*n* = 28 (35.00 %)	2.73 ± 1.37 %	2.67 (1.94 %)	0.68
40–59 Years	*n* = 22 (27.50 %)	2.31 ± 1.39 %	2.08 (2.11 %)	0.61
≥ 60 Years	*n* = 4 (5.00 %)	3.90 ± 0.97 %	4.20 (1.12 %)	0.88
Subgroup: Diagnosis				
ABC	*n* = 23 (28.75 %)	2.77 ± 1.37 %	2.93 (2.14 %)	0.04
GCT	*n* = 24 (30.00 %)	2.64 ± 1.38 %	2.44 (1.86 %)	0.99
Enchondroma	*n* = 9 (11.25 %)	2.22 ± 1.47 %	2.10 (2.27 %)	0.31
ACT	*n* = 5 (6.25 %)	2.69 ± 1.83 %	1.99 (3.02 %)	0.86
Chondroblastoma	*n* = 7 (8.75 %)	2.44 ± 1.22 %	2.55 (1.57 %)	0.10
CMF	*n* = 4 (5.00 %)	3.94 ± 0.72 %	4.13 (0.91 %)	0.55
Osteoblastoma	*n* = 2 (2.50 %)	2.88 ± 2.53 %	2.88 (1.79 %)	N/A
Unspecified	*n* = 6 (7.50 %)	2.84 ± 2.23 %	3.36 (3.86 %)	0.24

3.2. CT and MRI

Linear dimensions (X, Y, and Z) of the intraosseous defects were compared between CT- and MRI-derived 3D models. For the X-dimension, the absolute differences ($X_{CT - X_{MRI}}$) ranged from 0.03 to 37.72 mm, with a mean absolute difference of 0.64 mm (SD = 7.36 mm) and a median of 0.20 mm; the ICC was 0.92. For the Y-dimension, absolute differences ranged from 0.07 to 20.19 mm, with an absolute mean of 0.40 mm (SD = 5.02 mm) and a median of 0.06 mm; the ICC was 0.97. For the *Z*-dimension, the absolute differences ranged from 0.11 to 21.11 mm, with an absolute mean difference of 0.31 mm (SD = 5.82 mm) and a median of 0.48 mm; the ICC was 0.99.

The comparison of the measured volumes of the extracted 3D models from CT and MRI is visualized in Fig. 3A. The measured volumes derived from both CT and MRI scans were found to be non-normally distributed. The mean and SD of the V_R were 2.68 ± 1.44 %, with a range of 0.08 % to 4.99 %. The mean and the SD of the relative volume differences between the cavitary defects were 577.11 ± 709.10 mm^3, with a range from 0.87 mm^3 to 4103.62 mm^3. Relative volume differences of less than 1000 mm^3 were observed in the carpal and pelvic regions, whereas differences exceeding 1000 mm^3 were in long bones, such as the femur and tibia, particularly in cases involving large bone tumors. The Wilcoxon signed-rank test indicated no significant difference in the volume of the cavitary bone defects between the segmented CT and MRI scans ($p = 0.14$). The mean and SD of the average geometric surface deviation between the segmented CT and MRI scans was 0.14 ± 0.21 mm (Table 2). Multiple linear regression analysis revealed sex ($p = 0.51$), age ($p = 0.98$), and diagnostic groups ($p = 0.50$) did not have significant effects on the relative volume difference between the segmented CT and MRI scans of cavitary bone defects (Table 3).

3.3. Subgroups (sex, age, and diagnostics)

The comparison of the measured volumes of the extracted 3D models from CT and MRI of the subgroups are visualized in Fig. 3B-D. No significant difference was found between the 3D models derived from CT and MRI scans in both male ($p = 0.18$) and female ($p = 0.43$) groups, as assessed by the Wilcoxon signed-rank test. Similarly, no significant differences were observed across age groups: 0–19 years ($p = 0.12$), 20–39 years ($p = 0.68$), 40–59 years ($p = 0.61$) and over 60 years ($p = 0.88$). In the ABC diagnostic subgroup, segmented volumes from CT scans were significantly larger ($p = 0.04$) than those segmented from MRI scans. In contrast, no significant differences were found for other diagnostic subgroups, including GCT ($p = 0.99$), enchondroma ($p = 0.31$), ACT ($p = 0.86$), chondroblastoma ($p = 0.10$), CMF ($p = 0.55$) and unspecified bone lesions ($p = 0.24$), when analyzed using both the Wilcoxon signed-rank test and paired *t*-test. For the osteoblastoma subgroup, statistical significance could not be calculated due to the small sample size ($n = 2$) (Table 1).

3.4. Interobserver analysis

Interobserver segmentation reproducibility was excellent overall (Table 4, Table 5), as demonstrated by very high ICCs for both CT (ICC ≈ 0.99) and MRI (ICC ≈ 0.99) volumetric measurements. Despite this, paired analyses revealed a statistically significant difference in CT volumes, with a mean difference of 232.50 mm^3 (SD = 48.60 mm^3)—equivalent to roughly 1.10 %—and a large effect size ($r = 0.60$; $p = 0.002$–0.004), indicating that one observer consistently measured

Table 2
Demographic and clinical characteristics of the study population ($N = 80$), along with the V_{CT}, V_{MRI}, absolute difference of V_{CT} and V_{MRI}, and the measured surface deviation between 3D models extracted from CT and MRI scans. V_{CT}: measured volume of the 3D model extracted from CT; V_{MRI}: measured volume of the 3D model extracted from MRI; V_R: volume ratio; Min.: minimum; Max.: maximum; SD: standard deviation; GCT: giant cell tumor; ABC: aneurysmal bone cyst; ACT: atypical cartilaginous tumor; CMF: chondromyxoid fibroma; CCC: concordance correlation coefficient.

Patient	Sex	Age	Diagnosis	Linear Dimension Difference (CT – MRI)			Measured Volume				Surface Deviation (mm)			
				X (mm)	Y (mm)	Z (mm)	V_{CT} (mm^3)	V_{MRI} (mm^3)	Absolute Volume Difference (V_{CT} –V_{MRI}) (mm^3)	V_R	Min.	Max.	Mean	SD
1	M	23	GCT	2.1106	−7.0299	1.1985	51,522.40	53,847.60	2325.20	4.51 %	−4.07	4.20	0.22	1.64
2	M	22	ABC	−6.6298	−8.4646	7.6289	19,128.20	18,690.94	437.26	2.29 %	−2.82	3.14	−0.03	0.96
3	M	59	ACT	−14.2214	−3.8632	0.5068	20,804.42	21,217.83	413.41	1.99 %	−3.56	4.16	0.11	1.51
4	M	43	GCT	−1.3678	0.8	9.6625	10,704.54	10,487.93	216.61	2.02 %	−3.06	3.06	0.22	1.51
5	F	32	ABC	1.1137	−7.7295	−0.6281	120,923.81	116,820.20	4103.61	3.39 %	−7.26	7.23	0.06	2.68
6	F	34	GCT	−0.1047	−1.4967	2.4164	4871.97	4666.05	205.92	4.23 %	−2.00	2.01	−0.01	0.86
7	M	35	GCT	−0.6375	0.5727	4.6719	98,404.33	99,435.23	1030.90	1.05 %	−5.63	5.63	0.68	2.46
8	M	15	CMF	3.3158	−1.7239	4.5976	19,981.38	20,877.30	895.92	4.48 %	−3.25	3.43	0.41	1.46
9	M	45	ACT	1.7905	−1.6321	−0.676	23,975.13	23,593.81	381.33	1.59 %	−3.81	3.78	0.26	1.29
10	M	21	ABC	−5.6204	0.4514	−0.6045	3812.89	3961.29	148.39	3.89 %	−1.59	2.00	0.12	0.64
11	F	27	GCT	−3.4609	2.2436	3.9173	10,905.59	10,512.92	392.66	3.60 %	−2.29	2.93	−0.06	0.83
12	F	16	ABC	1.3597	−0.8687	1.4953	6931.88	6608.51	323.37	4.66 %	−2.21	2.24	0.17	0.87
13	M	64	Enchondroma	0.9011	−2.6131	3.4396	4875.98	4690.83	185.15	3.80 %	−2.59	2.59	0.13	1.09
14	M	57	CMF	−0.1968	0.8024	0.3992	11,897.25	11,360.73	536.52	4.51 %	−2.70	2.69	−0.04	0.82
15	F	78	GCT	1.9533	3.9525	6.9067	70,776.07	68,956.16	1819.91	2.57 %	−6.04	6.21	0.07	1.81
16	F	21	Chondroblastoma	0.2237	−2.5747	0.807	2402.15	2331.41	70.75	2.95 %	−1.68	1.68	0.08	0.80
17	M	64	ACT	−2.4163	0.795	3.4759	6342.99	6636.75	293.76	4.63 %	−2.45	2.47	0.63	0.95
18	M	45	ABC	−4.1752	−2.6657	7.154	78,023.35	77,500.20	523.15	0.67 %	−5.32	5.30	−0.02	1.39
19	M	13	CMF	0.8296	3.2556	−4.2536	3851.25	3706.10	145.15	3.77 %	−1.92	1.87	0.08	0.74
20	M	22	GCT	−0.9635	−8.4352	3.804	68,824.79	70,093.79	1269.00	1.84 %	−4.97	4.98	0.15	1.80
21	M	18	ABC	0.8755	5.3162	−0.9205	15,883.73	15,261.73	622.00	3.92 %	−2.80	2.79	−0.02	1.03
22	M	37	GCT	4.6675	1.4895	2.4084	57,208.75	54,970.93	2237.81	3.91 %	−4.95	4.75	−0.12	1.21
23	M	24	ABC	−9.3445	1.5116	3.8316	9468.42	9552.19	83.77	0.88 %	−2.64	2.65	0.17	0.90
24	M	61	Enchondroma	−1.1862	−5.8177	3.242	3305.47	3457.74	152.27	4.61 %	−1.89	1.89	0.19	0.92
25	F	43	Enchondroma	3.083	−1.514	1.8323	1790.94	1817.77	26.83	1.50 %	−1.59	1.59	0.21	0.70
26	M	53	ABC	2.2648	4.3432	−6.5231	9134.74	8807.11	327.63	3.59 %	−2.31	2.53	−0.01	0.74
27	M	18	ABC	−6.0717	−0.0852	−0.2613	6207.08	5947.62	259.47	4.18 %	−2.18	2.18	0.21	1.00
28	M	55	GCT	0.027	6.4732	−2.4513	6925.61	7170.74	245.13	3.54 %	−2.20	2.20	0.31	0.94
29	M	35	Unspecified	3.4162	−8.6191	−3.4669	9369.39	9582.34	212.96	2.27 %	−2.87	2.87	0.30	1.26
30	F	26	ABC	1.0784	−20.192	−21.1055	33,205.37	32,280.28	925.10	2.79 %	−4.86	6.22	0.00	1.64
31	M	29	ACT	1.3875	0.3939	5.9934	9928.99	9471.07	457.93	4.61 %	−2.75	3.17	−0.01	1.19
32	F	31	GCT	2.6421	0.9387	2.7245	12,990.76	12,667.01	323.74	2.49 %	−2.46	2.76	0.10	0.70
33	M	20	GCT	−1.147	−3.6664	−0.1243	37,976.21	37,142.61	833.60	2.20 %	−4.60	4.64	0.75	1.42
34	M	30	ABC	5.7968	4.3469	2.4625	12,119.53	12,484.89	365.35	3.01 %	−3.57	3.59	0.25	1.60
35	F	18	ABC	2.6038	1.2244	−0.5605	4905.49	5020.94	115.44	2.35 %	−2.68	2.68	0.57	1.18
36	M	45	GCT	2.1949	8.101	4.7743	59,762.62	58,711.37	1051.25	1.76 %	−5.39	5.35	0.35	1.75
37	F	52	GCT	0.4464	5.9414	−1.8814	25,993.78	26,615.66	621.88	2.39 %	−3.85	3.91	0.19	1.38
38	F	43	ABC	1.5676	3.1667	2.9321	12,476.15	11,998.89	477.26	3.83 %	−3.05	3.17	0.00	1.30
39	M	48	Enchondroma	−7.2152	4.9148	−0.8565	26,579.64	25,634.02	945.62	3.56 %	−3.66	3.59	−0.13	1.23
40	M	15	ABC	−0.8589	3.4726	−7.9746	26,934.98	25,677.96	1257.02	4.67 %	−3.22	3.76	−0.16	0.81
41	M	41	GCT	−0.5248	−0.6505	0.8222	6400.49	6548.66	148.18	2.32 %	−2.08	2.08	0.09	0.80
42	M	19	GCT	0.6837	−11.1719	−8.5728	100,172.02	100,852.21	680.20	0.68 %	−5.51	5.50	0.20	2.90
43	M	16	Chondroblastoma	1.3109	6.5152	1.8429	470.18	477.28	7.10	1.51 %	−0.92	0.91	0.04	0.46
44	F	56	Unspecified	−2.2844	−10.8242	−5.8635	1022.74	1068.13	45.39	4.44 %	−1.37	1.37	0.11	0.49
45	F	37	ACT	1.8375	−0.3499	2.8526	4841.49	4811.31	30.18	0.62 %	−2.01	2.01	0.27	1.00
46	M	12	ABC	34.7044	9.0823	−5.3239	89,857.82	87,303.40	2554.43	2.84 %	−6.51	4.26	−0.75	2.34
47	M	21	Chondroblastoma	−0.9261	−0.5175	0.9546	2083.38	2136.53	53.15	2.55 %	−1.45	1.45	0.15	0.63
48	M	28	GCT	1.7849	−1.7523	−3.7104	33,453.11	33,719.35	266.24	0.80 %	−3.51	3.49	0.09	1.48
49	F	18	ABC	3.0415	−0.0738	−0.6283	20,090.32	20,202.79	112.47	0.56 %	−3.34	3.36	0.20	1.39
50	M	18	ABC	1.4342	1.5127	3.9198	42,147.95	41,158.81	989.15	2.35 %	−4.47	4.47	0.06	1.78

(*continued on next page*)

Table 2 (*continued*)

Patient	Sex	Age	Diagnosis	Linear Dimension Difference (CT – MRI)			Measured Volume				Surface Deviation (mm)			
				X (mm)	Y (mm)	Z (mm)	V_{CT} (mm^3)	V_{MRI} (mm^3)	Absolute Volume Difference (V_{CT} –V_{MRI}) (mm^3)	V_R	Min.	Max.	Mean	SD
51	F	13	Unspecified	3.5637	9.228	−9.8897	445.23	466.71	21.48	4.83 %	−1.57	1.56	0.05	0.90
52	M	10	ABC	4.752	−2.5209	0.1932	11,720.54	12,199.27	478.72	4.08 %	−3.13	3.21	−0.02	1.17
53	F	41	GCT	−4.2257	−5.2214	−1.4847	45,179.12	47,259.13	2080.01	4.60 %	−3.64	4.19	0.46	1.29
54	M	16	ABC	−0.7718	−3.9747	−1.7803	7497.03	7449.26	47.77	0.64 %	−2.54	2.54	0.09	0.91
55	F	16	ABC	0.1695	−2.2359	−7.8987	9632.97	9757.07	124.10	1.29 %	−2.68	2.69	0.13	1.25
56	F	18	ABC	−7.0647	1.2302	2.15	66,649.55	65,379.98	1269.57	1.90 %	−5.37	5.34	−0.04	1.74
57	M	19	GCT	0.0605	−1.3346	−0.8927	52,392.30	50,527.83	1864.47	3.56 %	−4.14	4.14	−0.21	1.99
58	F	41	Enchondroma	−0.4396	1.6697	6.4036	2686.53	2629.20	57.33	2.13 %	−1.68	1.67	0.02	0.72
59	F	46	Chondroblastoma	4.1197	−0.3809	−2.4005	11,023.56	10,916.76	106.80	0.97 %	−2.95	2.96	0.12	1.49
60	F	58	ABC	1.084	4.7591	2.0939	3705.57	3652.66	52.90	1.43 %	−2.24	2.30	0.15	0.92
61	F	20	Unspecified	0.3883	1.9123	3.0385	4496.29	4490.84	5.45	0.12 %	−2.19	2.46	0.14	0.97
62	M	19	Osteoblastoma	−0.6359	−1.1363	3.2195	1308.89	1294.58	14.31	1.09 %	−1.22	1.21	0.17	0.50
63	F	14	Chondroblastoma	1.1415	−3.4848	0.4627	327.10	322.29	4.81	1.47 %	−0.76	0.81	0.17	0.39
64	F	22	Unspecified	−3.6831	4.8161	0.1095	18,500.70	19,423.89	923.18	4.99 %	−2.42	3.60	0.30	0.92
65	M	41	GCT	−27.8328	−2.6265	1.2694	146,912.40	146,795.68	116.72	0.08 %	−6.63	6.70	0.06	2.19
66	F	49	Enchondroma	−37.7176	−3.0911	−1.976	23,200.10	23,297.50	97.41	0.42 %	−3.07	3.07	0.22	1.17
67	F	28	GCT	6.6717	0.5368	−16.4239	36,274.30	37,375.56	1101.26	3.04 %	−3.86	4.30	0.22	1.02
68	M	11	Chondroblastoma	−3.5675	0.9259	−4.3548	5895.16	5708.21	186.95	3.17 %	−1.96	1.91	0.06	1.03
69	M	15	ABC	−0.137	6.7592	−6.1116	28,159.24	29,160.47	1001.22	3.56 %	−4.01	4.02	0.24	1.42
70	M	20	Enchondroma	−2.7426	−3.0653	−7.9494	23,412.37	23,110.68	301.70	1.29 %	−5.74	5.80	0.40	1.86
71	M	47	Enchondroma	−5.8265	0.5732	18.0778	39,627.81	39,860.69	232.87	0.59 %	−5.46	5.46	0.29	1.31
72	F	54	CMF	5.5638	5.3636	−3.3558	22,975.21	23,664.24	689.03	3.00 %	−3.67	3.67	0.16	1.18
73	F	14	Osteoblastoma	0.2595	−0.4483	−2.2247	2314.08	2205.93	108.15	4.67 %	−1.52	1.55	−0.04	0.85
74	F	32	GCT	−0.8901	1.9466	2.006	20,162.75	21,038.64	875.90	4.34 %	−2.49	3.12	0.29	1.04
75	M	38	GCT	2.1486	−1.1245	16.4358	51,383.32	50,359.44	1023.88	1.99 %	−4.57	4.92	−0.05	1.24
76	F	16	Unspecified	0.0689	−1.7896	−0.6206	214.08	213.21	0.87	0.40 %	−0.65	0.66	−0.02	0.30
77	M	15	Chondroblastoma	1.4892	5.0476	−0.176	3063.06	2936.57	126.49	4.13 %	−1.79	1.80	0.20	0.81
78	F	15	GCT	−3.4522	−13.6019	14.0594	43,536.74	43,126.53	410.21	0.94 %	−4.75	4.87	0.39	1.71
79	F	39	Enchondroma	−0.1696	1.4108	−4.4033	7282.30	7129.63	152.67	2.10 %	−2.26	2.25	0.01	0.84
80	M	24	GCT	−4.273	0.2028	1.0183	11,422.03	10,876.25	545.78	4.78 %	−2.72	2.73	0.03	0.95
Min.				**0.027**	**0.0738**	**0.1095**	**214.08**	**213.21**	**0.87**	**0.08 %**	**−7.26**	**0.66**	**−0.75**	**0.30**
Max.				**−37.7176**	**−20.192**	**−21.1055**	**146,912.40**	**146,795.68**	**4103.61**	**4.99 %**	**−0.65**	**7.23**	**0.75**	**2.90**
Mean		**31.43**		**−0.635691**	**−0.404614**	**0.3110338**	**25,288.35**	**25,139.69**	**577.11**	**2.68 %**	**−3.19**	**3.28**	**0.14**	**1.20**
SD		**16.02**		**7.35754374**	**5.01870845**	**5.82118318**	**29,811.47**	**29,558.24**	**709.10**	**1.44 %**	**1.48**	**1.46**	**0.21**	**0.51**
Median		**27.5**		**0.1966**	**0.0645**	**0.48475**	**12,008.39**	**12,099.08**	**323.56**	**2.56 %**	**−2.81**	**3.07**	**0.13**	**1.13**
CCC							**0.9995**							
ICC				**0.923842744**	**0.96638973**	**0.99459359**								
***p*-value**							**0.14**							

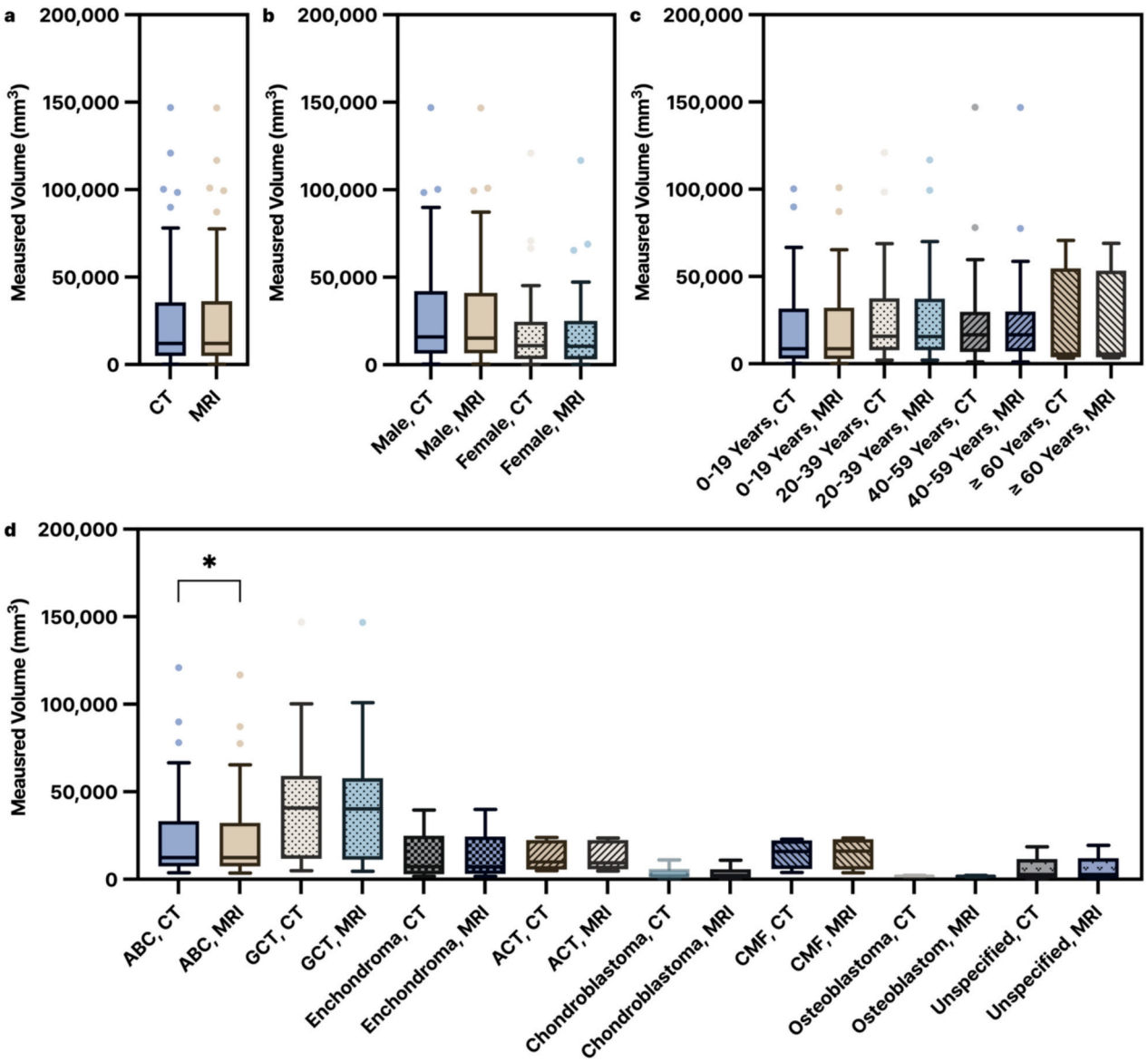

Fig. 3. Graphical presentation of the measured volumes of the extracted 3D models for (A) CT and MRI comparison, and again in (B) sex subgroups, (C) age subgroups, and (D) diagnosis subgroups. ABC: aneurysmal bone cyst; GCT: giant cell tumor; ACT: atypical cartilaginous tumor; CMF: chondromyxoid fibroma.

Table 3
Multiple linear regression analysis ($R^2 = 0.0104$, F-statistic = 0.2657 ($p = 0.85$), and degrees of freedom = 76) of V_R and subgroups. V_R: volume ratio; CI: confidence interval.

Variables	Coefficient (β)	Standard Error	*t*-value	*p*-value	95 % CI
Intercept (β_0)	0.0268	0.0041	6.6240	< 0.0001	[0.0187, 0.0349]
Sex (β_1)	−0.0022	0.0034	0.6699	0.51	[−0.0089, 0.0042]
Age (β_2)	−0.000002	0.0001	0.0197	0.98	[−0.0002, 0.0002]
Diagnosis (β_3)	0.0005	0.0008	0.6785	0.50	[−0.0010, 0.0021]

slightly larger volumes. Bland–Altman analysis further confirmed this trend, demonstrating that observer 1 consistently reported greater CT volumes than observer 2, as indicated by the positive mean differences. In contrast, MRI volume differences were not statistically significant ($p > 0.10$) despite a moderate numerical discrepancy between medians ($\Delta 928.40\ mm^3$, ~2.60 %). Analysis of linear dimensions showed that CT X- and Y-measurements were highly consistent (ICC = 0.99 and 0.99, respectively; $p = 0.10$ and 0.87), while the CT Z-dimension exhibited a small but significant interobserver difference ($p = 0.03$, $r = 0.47$), averaging at approximately 2.16 mm. For MRI, although the Y-dimension did not differ significantly ($p = 0.17$), both the X- and Z-dimensions showed significant discrepancies between observers—most notably, the MRI Z-dimension ($p = 0.01$, $r = 0.54$), which differed by approximately 2.4 mm. Bland–Altman analyses corroborated these findings, revealing generally balanced differences with a few outliers, particularly indicating a tendency for second observer's measurements in the MRI X- and CT Z-dimensions.

4. Discussion

Preoperative planning using 3D modelling based on biomedical imaging scans has garnered significant attention in orthopedic surgery, particularly for managing complex cavitary bone defects. Accurate imaging is critical for planning resection, ensuring proper reconstruction, and minimizing postoperative complications. Traditionally, diagnostic

Table 4
Demographic and clinical characteristics of the IOA population ($N = 30$), along with the V_{CT}, V_{MRI}, absolute difference of V_{CT} and V_{MRI}, and the measured surface deviation between 3D models extracted from CT and MRI scans. V_{CT}: measured volume of the 3D model extracted from CT; V_{MRI}: measured volume of the 3D model extracted from MRI; V_R: volume ratio; ABC: aneurysmal bone cyst; GCT: giant cell tumor; CMF: chondromyxoid fibroma.

Patient	Sex	Age	Diagnosis	Linear Dimension Difference (CT – MRI)			Measured Volume			
				X (mm)	Y (mm)	Z (mm)	V_{CT} (mm^3)	V_{MRI} (mm^3)	Absolute Volume Difference (V_{CT} –V_{MRI}) (mm^3)	V_R
41	M	41	GCT	−4.3677	−2.2691	−0.6549	5900.3315	6059.4663	159.1348	2.697048
51	F	13	Unspecified	0.3835	11.5343	−9.7457	443.9601	458.161	14.2009	3.198688
52	M	10	ABC	3.5385	−4.2536	1.2491	12,354.0674	13,127.6953	773.6279	6.262131
53	F	41	GCT	1.5419	−1.656	0.5386	43,000.543	44,044.1406	1043.598	2.426941
54	M	16	ABC	−0.4402	−2.9186	6.891	7385.4961	7378.1768	7.3193	0.099104
55	F	16	ABC	0.9385	5.6987	−7.0477	8755.9492	8516.0879	239.8613	2.739409
56	F	18	ABC	−1.6795	2.1746	2.7415	65,308.082	64,238.2109	1069.871	1.638191
57	M	19	GCT	−1.814	−2.1009	1.4298	50,574.1484	50,959.1797	385.0313	0.76132
58	F	41	Enchondroma	0.6459	0.674	1.4467	2708.925	2701.125	7.8	0.287937
59	F	46	Chondroblastoma	3.5403	−2.2278	7.9341	10,379.0596	10,484.8398	105.7802	1.019169
60	F	58	ABC	−1.7388	1.5782	1.7949	3703.2644	3809.4785	106.2141	2.868121
61	F	20	Unspecified	−0.8238	0.9167	−1.1182	4520.2573	4668.9849	148.7276	3.290246
62	M	19	Osteoblastoma	−1.278	3.1815	2.1057	1545.5837	1585.6764	40.0927	2.594017
63	F	14	Chondroblastoma	−0.0811	0.0092	0.8361	319.019	322.6677	3.6487	1.143725
64	F	22	Unspecified	−2.3887	2.7962	−0.0381	18,024.584	18,466.1777	441.5937	2.449952
65	M	41	GCT	−0.537	−1.2026	0.6719	145,274.1563	145,935.9063	661.75	0.455518
66	F	49	Enchondroma	−0.4266	−0.1501	−3.1067	22,504.9648	23,975.4785	1470.514	6.534175
67	F	28	GCT	5.5703	3.9513	−0.5517	35,716.8789	34,517.6406	1199.238	3.357623
68	M	11	Chondroblastoma	−2.6847	−2.0382	0.2962	5364.9902	5231.4399	133.5503	2.489293
69	M	15	ABC	−0.5401	−0.1445	−1.1424	28,175.3594	27,994.4238	180.9356	0.642177
70	M	20	Enchondroma	3.319	5.7188	1.2355	22,919.959	23,167.6172	247.6582	1.080535
71	M	47	Enchondroma	−4.3837	0.9932	−0.0944	38,794.707	38,219.3945	575.3125	1.482966
72	F	54	CMF	1.0514	1.1393	0.4683	22,568.6719	22,139.6465	429.0254	1.900978
74	F	32	GCT	−1.9961	−0.2774	1.5161	21,847.5039	21,270.2734	577.2305	2.642089
75	M	38	GCT	−0.712	1.6702	−1.0914	51,042.9961	51,658.9336	615.9375	1.206703
76	F	16	Unspecified	2.5391	−2.8476	0.1109	216.4172	217.733	1.3158	0.607992
77	M	15	Chondroblastoma	0.6887	2.571	−0.3984	3007.3096	3276.6453	269.3357	8.956035
78	F	15	GCT	−0.9512	−3.8748	−0.0106	43,775.4023	42,687.5781	1087.824	2.485012
79	F	39	Enchondroma	1.1206	0.1196	0.7227	7199.5776	7204.4341	4.8565	0.067455
80	M	24	GCT	−0.7181	1.6038	1.6064	10,966.0166	11,234.5107	268.4941	2.44842

Table 5
IOA Analysis comparing volume and linear dimensions (X, Y, and Z) of a subsample of patients ($n = 30$). IOA: interobserver agreement; CT: computed tomography; MRI: magnetic resonance imaging

	Volume (mm^3)		X Dimension (mm)		Y Dimension (mm)		Z Dimension (mm)	
	CT	MRI	CT	MRI	CT	MRI	CT	MRI
Average Difference Volume	372.9517	380.6571	0.5129	2.8479	0.0657	0.7399	2.1609	2.3927
Std Differences Volume	740.4790	1009.1812	1.6624	8.7641	2.1202	2.4753	5.1747	4.9952
Upper Level of Agreement	1824.2905	2358.6522	3.7712	20.0255	4.2212	5.5916	12.3034	12.1833
Lower Level of Agreement	−1078.3872	−1597.3380	−2.7454	−14.3298	−4.0898	−4.1117	−7.9815	−7.3979
Minimum	215.2469	215.4714	9.0269	7.7229	6.8440	9.1626	7.2921	7.5469
Maximum	146,093.2777	146,365.7949	72.2179	86.4028	56.9748	54.5597	109.1986	112.5555
Intraclass Correlation Coefficient	0.9996	0.9993	0.9925	0.8547	0.9868	0.9818	0.9794	0.9785
p-value	0.0032	0.1579	0.1018	0.1901	0.8664	0.1124	0.0248	0.0092

practices have relied on X-ray, CT, and MRI to guide surgical strategies. Among these, CT is often preferred due to its superior spatial resolution, allowing for detailed visualization of bone structures. However, CT's limitations, such as ionizing radiation exposure and difficulty distinguishing between soft tissues, are significant concerns, especially in pediatric and repeat-scan cases.

This study aimed to assess the feasibility of MRI as an alternative imaging modality for preoperative segmentation and planning of cavitary bone defects. Given MRI's superior soft tissue contrast, widespread clinical use, and the absence of radiation, it presents a compelling case for replacing CT in specific surgical scenarios. We hypothesize that MRI, despite its lower spatial resolution, will produce volumetric and surface measurements for cavitary bone defects within an acceptable clinical threshold compared to CT, making it a viable alternative in modern healthcare practice.

In evaluating cavitary bone defects, imaging modalities such as CT and MRI play a crucial role in tumor staging, volume estimation, and assessing impact on surrounding tissues [30]. The choice of imaging modality is often influenced by specific diagnostic and surgical goals. CT is traditionally favored due to its ability to assess cortical bone integrity, calcifications, and detect recurrent bony defects [31]. However, CT exposes patients to high doses of ionizing radiation—up to 100–1000 times greater than conventional radiography [31], which is particularly problematic in pediatric cases or those requiring frequent monitoring. In previous research, it has been attempted to estimate the volume of cavitary bone defects using radiographs [32]. While radiographs can estimate cavitary defect volume through a simplified ellipsoidal volume formula $\frac{3}{4}\pi \times \frac{a}{2} \times \frac{b}{2} \times \frac{c}{2}$, where a, b, and c correspond to length, width, and depth [32], this method often underestimates volume, particularly in cases of irregular geometries, as demonstrated in Deventer et al.'s [33] work on ABC. Consequently, more advanced imaging modalities like CT and MRI are needed for accurate volumetric estimation, particularly for

complex cases.

While CT is excellent for bone visualization, MRI offers superior soft tissue contrast, making it invaluable for differentiating between pathologies that may appear similar on radiographs, such as ABC-similar variants, telangiectatic osteosarcoma [34,35]. MRI's advantage in soft tissue imaging is particularly important for tumor staging and assessing extraosseous extension [36,37], which can significantly alter surgical planning. As MRI is particularly effective at measuring the volume of extraosseous extension compared to CT, for the purpose of this study and to ensure the specific comparison of segmentation accuracy, it was decided to exclude cases of this nature.

A key challenge in preoperative planning is achieving precise surgical margins. Inadequate margin control can increase the risk of local recurrence or metastasis, particularly in local aggressive tumors like sarcomas [38]. For benign lesions, however, intralesional curettage is typically the standard approach. While CT is the traditional choice for pre-surgical imaging, recent studies indicate that MRI provides sufficient detail for delineating tumor boundaries and joint involvement in benign and local aggressive primary lesions, such as ABC and GCT [23,39,40]. Importantly, MRI's ability to delineate tumor margins relative to soft tissues provides critical information that CT may miss [39].

Our study shows that MRI could serve as a viable alternative to CT in preoperative planning for cavitary bone defects. The average relative volume difference between CT and MRI was 2.68 ± 1.44 %, which is clinically insignificant. Furthermore, the average geometric surface deviation between 3D models generated from CT and MRI scans was 0.14 ± 0.21 mm, which falls well within the 5 mm surgical tolerance threshold [41]. In addition, our linear dimension analysis revealed minimal mean differences in the X (length), Y (width), and Z (depth) dimensions (−0.64 mm, −0.40 mm, and 0.31 mm, respectively) with median differences close to zero. Although the absolute ranges and standard deviations were wider (up to 37.72 mm with SDs of 7.36, 5.02, and 5.82 mm for X, Y, and Z), this variability is primarily due to outlier floating-point precision errors in segmentation, particularly in defects with multiple sections. Nevertheless, the excellent interclass correlation between the linear dimensions of CT and MRI derived models (ICC values of 0.92, 0.97, and 0.99 for X, Y, and Z) confirms the agreement of these measurements. Collectively, these results indicate a high degree of concordance between the two modalities despite MRI's lower spatial resolution.

Interestingly, MRI segmentations tended to overestimate surface boundaries compared to CT, though overall volume was underestimated. This pattern aligns with findings from similar studies and can be attributed to differences in the modalities' characteristics [42]. CT, with its superior spatial resolution, allows for more accurate segmentation of bone morphology, while MRI, with its superior soft tissue contrast, provides better delineation of tumor margins in relation to surrounding tissues such as muscle and fat [43]. This trade-off must be carefully considered during preoperative planning, particularly for lesions close to critical structures and when stability criteria come into play.

The "staircasing" effect in MRI-based 3D models, caused by lower spatial resolution and anisotropic voxel sizes, contributed to the surface deviations. However, this effect did not significantly affect volumetric estimations, as evidenced by the relatively small relative volume differences between CT and MRI (ranging from 0.87 to 4103.62 mm^3, with a median of 323.56 mm^3). The positive correlation between lesion size and volume difference highlights that surface deviations remain constant while overall volume increases.

In subgroup analyses, significant volumetric discrepancies were observed in the ABC subgroup. This subgroup displayed statistically significant volume discrepancies between CT and MRI scans ($p = 0.04$), with an absolute volumetric ratio of 2.77 ± 1.37 %. This is likely due to the varying internal structure of ABCs, which feature multiple cystic spaces filled with blood and fibrous septa [44], leading to different measurements between CT and MRI scans [45,46]. This finding reinforces the idea that MRI is particularly useful in identifying soft tissue components that may be obscured on CT.

Epidemiologically, benign and local aggressive primary bone tumors like ABC and GCT are more common in males and younger patients, although these differences are not statistically significant [47]. Our study confirmed that volumetric ratios were larger in male and younger subgroups, but multiple regression analysis showed no significant influence of these demographic factors on volume differences between CT and MRI (sex: $p = 0.51$, age: $p = 0.98$, and diagnosis: $p = 0.50$). This suggests that the imaging modality's characteristics, rather than patient demographics, primarily affect segmentation accuracy. A conclusion that aligns with prior works, indicating that MRI's soft tissue contrast and segmentation precision are largely dependent on technical factors such as voxel size and imaging protocols [48,49].

Previous research has also highlighted that varying imaging protocols for CT and MRI can significantly influence 3D segmentation results [48]. Factors such as weak tissue boundaries, noise, intensity inhomogeneity, and partial volume effects in MRI contribute to segmentation inconsistencies [50]. Most MRI scans in our study were more anisotropic with larger slice sizes compared to CT, leading to lower spatial resolution and poorer boundary delineation of bone defects [51]. These partial volume effects particularly may impact the accuracy of bone segmentation in complex bone structures with high joint proximity [52].

Our analysis was restricted to intraosseous tumors to ensure methodological precision and clinical relevance. While MRI excels in soft tissue contrast, its limited spatial resolution impedes reliable delineation of cortical breaches, which are better visualized on CT. Including extraosseous components risked conflating soft tissue invasion with true osseous defects, potentially distorting volumetric accuracy. By prioritizing intraosseous defects—common in benign and locally aggressive lesions such as ABC and GCT—we focused on scenarios where MRI's strengths (e.g., radiation-free soft tissue discrimination) directly align with surgical objectives like intralesional curettage. MRI's superior ability to differentiate cystic septations, fluid-fluid levels, and intramedullary margins offers distinct advantages over CT for these lesions, even when cortical assessment is deferred. This approach underscores MRI's utility in contexts where soft tissue contrast outweighs the need for cortical detail, isolating its value in defining cancellous tumor geometry while circumventing ambiguities introduced by extraosseous or cortical evaluation. Ultimately, this ensures our findings remain clinically actionable, providing reliable preoperative insights for targeted intralesional surgery.

Manual segmentation, used in this study, is time-consuming and subject to operator bias [53,54], particularly for MRI, where standard segmentation algorithms are less developed compared to CT [55,56]. Further, this technique subject to operator bias, as Yepes-Calderon et al. [53] suggested, manually segmented scans tend to exhibit high inter- and intra-operator variability and lack reproducibility, leading to potentially inaccurate outcomes. As there are no metrics for analyzing manually segmented volumes, which rely entirely on the experience of the radiologists or orthopedic surgeons, Fenster et al. [57] proposed three categories to evaluate segmentation analysis, including accuracy, precision as a measure of repeatability, and time efficiency. To measure this, several metrics were used in previous studies, such as dice similarity coefficient and volumetric similarity to evaluate the accuracy and reproducibility of segmentations of CT and MRI scans [58,59].

Further, IOA demonstrated that segmentation reproducibility was generally robust, with excellent ICCs for both CT (ICC ≈ 0.99) and MRI (ICC ≈ 0.99) volumetric measurements. However, paired analyses and Bland–Altman plots revealed significant interobserver variability in CT volumes and the Z dimensions of both CT and MRI scans. In particular, observer 1 consistently reported higher CT volumes than observer 2, as evidenced by a positive mean difference and statistically significant paired comparisons. While MRI volume differences did not reach

significance, the discrepancies in the MRI X and CT Z dimensions suggest the presence of systematic biases. These unexpected variations may be accentuated by differences in slice thickness and anisotropic voxel sizes—especially along the Z axis—leading to notable volume effects and variable boundary delineation. Despite these observed differences, the absolute interobserver discrepancies ranged only from approximately 0.07 mm to 2.80 mm on average, a distance well within the 5 mm surgical margin commonly employed in orthopedic procedures. Likewise, although some volumetric comparisons reached statistical significance, the relative differences remained below 3 %, which is unlikely to alter clinical decision-making. Given that manual segmentation is inherently operator-dependent, these findings underscore the need for standardized segmentation protocols and enhanced observer calibration. Nonetheless, because the observed disparities fall within clinically acceptable thresholds, our results confirm that both CT- and MRI-based 3D models remain reliable for precise preoperative planning.

In clinical practice, MRI can be a viable alternative to CT when the relative volume difference between the two modalities is less than 5 %. This threshold aligns with the typical allowance of 0–10 % free space which is typically permitted in orthopedic surgery, depending on the tumor's nature, location, and type of bone substitute [60]. This also aligns with Wu et al.'s [60] findings that certain characteristics, such as lesion size, location, and the degree of filling (> 90 %), affect healing outcomes. In cases where soft tissue involvement is a concern, MRI's superior contrast makes it an invaluable tool. Given that surgeons typically plan for a resection area larger than the actual bone cavity to prevent postoperative complications like recurrence [61], the minor volume differences observed in this study suggest that MRI is a safe and effective alternative to CT for managing cavitary bone defects in specific surgical contexts.

5. Conclusion

Accurate delineation of cavitary bone defects and surgical margins is paramount for effective preoperative planning. Historically, 3D models generated from CT scan segmentations have been considered the gold standard for this purpose. However, the inherent limitations of CT, such as ionizing radiation exposure and poor delineation between bony and soft tissue interfaces, necessitate the exploration of alternative imaging modalities. This study evaluated the efficacy of MRI-derived 3D models as a viable alternative for preoperative planning in the treatment of cavitary bone defects. Our findings affirm that MRI can serve as a practical substitute for CT in specific surgical contexts. The relative volume ratio discrepancy between CT and MRI scans was 2.68 ± 1.44 %, a clinically and statistically insignificant deviation. Additionally, surface deviations remained within acceptable surgical thresholds, falling below the 5 mm tolerance limit. These results suggest that, despite MRI's lower spatial resolution, its superior soft tissue contrast allows for the accurate identification of tumor margins, particularly in lesions such as ABC with complex internal structures. The minor volumetric differences observed in this study are likely attributable to technical factors such as partial volume effects and the staircasing phenomenon inherent to MRI voxel size, rather than patient demographic variables like age or sex. Furthermore, our IOA analysis demonstrated robust reproducibility for both CT- and MRI-based segmentations, reinforcing the reliability of MRI models for surgical planning. Therefore, MRI emerges as an effective alternative to CT in preoperative planning of volumetric estimations, especially in cases where soft tissue involvement is critical. These findings highlight MRI's potential as a valuable tool in the preoperative planning of cavitary bone defect treatment, enhancing the precision of planning while mitigating the risks associated with ionizing radiation exposure.

Funding

This research project was supported by Bayerisches Verbundforschungsprogramm (BayVFP) (Funding Indicator: LSB-2203-0005).

Institutional review board statement

This study was conducted in accordance with the Declaration of Helsinki and approved by the Ethics Committee of LMU Munich (ID: 23–0296).

CRediT authorship contribution statement

Yooseok Chae: Writing – review & editing, Writing – original draft, Validation, Methodology, Investigation, Data curation. **Giles Michael Cheers:** Writing – review & editing, Writing – original draft, Validation, Supervision, Methodology, Data curation, Conceptualization. **MinJoo Kim:** Writing – review & editing, Writing – original draft, Visualization, Validation, Supervision, Conceptualization. **Paul Reidler:** Writing – review & editing, Validation, Supervision, Data curation. **Alexander Klein:** Writing – review & editing, Validation, Supervision, Data curation. **Thomas Fevens:** Writing – review & editing, Supervision. **Boris Michael Holzapfel:** Writing – review & editing, Supervision, Project administration, Funding acquisition, Conceptualization. **Susanne Mayer-Wagner:** Writing – review & editing, Supervision, Project administration, Funding acquisition, Conceptualization.

Declaration of competing interest

The authors listed have no affiliation with or involvement for financial interests in the subject matter or materials discussed in this manuscript.

Acknowledgement

Nonapplicable.

Data availability

Upon request, standard operation protocol of the methodologies and files (excluding patient information) supporting this study's findings can be obtained from the corresponding authors.

References

[1] Choi JH, Ro JY. The 2020 WHO classification of tumors of bone: an updated review. Adv Anat Pathol 2021;28:119–38. https://doi.org/10.1097/pap.0000000000000293.
[2] Werner M. Giant cell tumour of bone: morphological, biological and histogenetical aspects. Int Orthop 2006;30:484–9. https://doi.org/10.1007/s00264-006-0215-7.
[3] Zhang H, Alman BA. Enchondromatosis and growth plate development. Curr Osteoporos Rep 2021;19:40–9. https://doi.org/10.1007/s11914-020-00639-7.
[4] Kim J-H, Lee SK. Classification of chondrosarcoma: from characteristic to challenging imaging findings. Cancers 2023;15:1703. https://doi.org/10.3390/cancers15061703.
[5] Perera JR, Saifuddin A, Pollock R. Management of benign bone tumours. Orthop Trauma 2017;31:151–60. https://doi.org/10.1016/j.mporth.2017.03.008.
[6] Franchi A. Epidemiology and classification of bone tumors. Clin Cases Miner Bone Metab 2012;9:92–5.
[7] Harrleson J. Bone tumors. Ann Surg 1980;191:511. https://doi.org/10.1097/00000658-198004000-00031.
[8] Mittra E, Iagaru A. 18F-FDG-PET and PET/CT for evaluating primary bone tumors. PET Clin 2010;5:327–39. https://doi.org/10.1016/j.cpet.2010.04.004.
[9] Tomasian A, Cazzato RL, Sharma K, et al. Benign bone tumors: state of the art in minimally invasive percutaneous interventions. RadioGraphics 2023;43:e220041. https://doi.org/10.1148/rg.220041.
[10] Errani C, Tsukamoto S, Mavrogenis AF. Imaging analyses of bone tumors. JBJS Rev 2020;8. https://doi.org/10.2106/jbjs.rvw.19.00077. e0077–e0077.
[11] Hakim DN, Pelly T, Kulendran M, Caris JA. Benign tumours of the bone: a review. J Bone Oncol 2015;4:37–41. https://doi.org/10.1016/j.jbo.2015.02.001.
[12] Motamedi K, Seeger LL. Benign bone tumors. Radiol Clin North Am 2011;49:1115–34. https://doi.org/10.1016/j.rcl.2011.07.002.
[13] Wolf RE, Enneking WF. The staging and surgery of musculoskeletal neoplasms. Orthop Clin North Am 1996;27:473–81. https://doi.org/10.1016/s0030-5898(20)32093-9.

[14] Fan B, Zhang J. A review of medical image segmentation techniques. Front Comput Intell Syst 2023;4:89–91. https://doi.org/10.54097/fcis.v4i3.11149.
[15] Requist MR, Mills MK, Carroll KL, Lenz AL. Quantitative skeletal imaging and image-based modeling in pediatric Orthopaedics. Curr Osteoporos Rep 2024;22:44–55. https://doi.org/10.1007/s11914-023-00845-z.
[16] Bone-RADS™ AC of RC on guidelines for specialist referral for newly identified bone lesions. https://www.msts.org/view/download.php/education/generalist-information-statement. [Accessed 29 July 2024].
[17] Liu Z, Kainth K, Zhou A, et al. A review of self-supervised, generative, and few-shot deep learning methods for data-limited magnetic resonance imaging segmentation. NMR Biomed 2024:e5143. https://doi.org/10.1002/nbm.5143.
[18] Goldman LW. Principles of CT and CT technology. J Nucl Med Technol 2007;35:115–28. https://doi.org/10.2967/jnmt.107.042978.
[19] Liu Z-Q, Liew HL, Clement JG, Thomas CDL. Bone image segmentation. IEEE Trans Biomed Eng 1999;46:565–73. https://doi.org/10.1109/10.759057.
[20] Zoroofi RA, Sato Y, Sasama T, et al. Automated segmentation of acetabulum and femoral head from 3-D CT images. IEEE Trans Inf Technol Biomed 2003;7:329–42. https://doi.org/10.1109/titb.2003.813791.
[21] Tangsiwong T, Phewplung T, Trinavarat P. Factors affecting high cumulative radiation exposure from paediatric computed tomography. Pol J Radiol 2021;86:e455–60. https://doi.org/10.5114/pjr.2021.108352.
[22] Chodick G, Kim KP, Shwarz M, et al. Radiation risks from pediatric computed tomography scanning. Pediatr Endocrinol Rev 2009;7:29–36.
[23] Hogeboom WR, Hoekstra HJ, Mooyaart EL, et al. MRI or CT in the preoperative diagnosis of bone tumours. Eur J Surg Oncol 1992;18:67–72.
[24] Thanacharoenpanich S, Bixby S, Breen MA, Kim Y-J. MRI is better than CT scan for detection of structural pathologies after traumatic posterior hip dislocations in children and adolescents. J Pediatr Orthop 2020;40:86–92. https://doi.org/10.1097/bpo.0000000000001127.
[25] Heckelman LN, Soher BJ, Spritzer CE, et al. Design and validation of a semi-automatic bone segmentation algorithm from MRI to improve research efficiency. Sci Rep 2022;12:7825. https://doi.org/10.1038/s41598-022-11785-6.
[26] Hamwood J, Schmutz B, Collins MJ, et al. A deep learning method for automatic segmentation of the bony orbit in MRI and CT images. Sci Rep 2021;11:13693. https://doi.org/10.1038/s41598-021-93227-3.
[27] Gitelis S, Wilkins R, Conrad EU. Benign bone tumors. J Bone Jt Surg 1995;77:1756–82. https://doi.org/10.2106/00004623-199511000-00018.
[28] Ritacco LE, Milano FE, Farfalli GL, et al. Virtual planning and allograft preparation guided by navigation for reconstructive oncologic surgery. JBJS Essent Surg Tech 2017;7:e30. https://doi.org/10.2106/jbjs.st.17.00001.
[29] Mavrogenis AF, Igoumenou VG, Megaloikonomos PD, et al. Giant cell tumor of bone revisited. SICOT-J 2017;3:54. https://doi.org/10.1051/sicotj/2017041.
[30] Board WC of TE. WHO classification of Tumours. 5th ed. Soft Tissue and Bone Tumours; 2020.
[31] Miwa S, Otsuka T. Practical use of imaging technique for management of bone and soft tissue tumors. J Orthop Sci 2017;22:391–400. https://doi.org/10.1016/j.jos.2017.01.006.
[32] Göbel V, Jürgens H, Etspüler G, et al. Prognostic significance of tumor volume in localized Ewing's sarcoma of bone in children and adolescents. J Cancer Res Clin Oncol 1987;113:187–91. https://doi.org/10.1007/bf00391442.
[33] Deventer N, Schulze M, Gosheger G, et al. Primary aneurysmal bone cyst and its recent treatment options: a comparative review of 74 cases. Cancers 2021;13:2362. https://doi.org/10.3390/cancers13102362.
[34] Zishan US, Pressney I, Khoo M, Saifuddin A. The differentiation between aneurysmal bone cyst and telangiectatic osteosarcoma: a clinical, radiographic and MRI study. Skeletal Radiol 2020;49:1375–86. https://doi.org/10.1007/s00256-020-03432-w.
[35] Docquier P-L, Paul L, Menten R, et al. Measurement of bone cyst fluid volume using k-means clustering. Magn Reson Imaging 2009;27:1430–9. https://doi.org/10.1016/j.mri.2009.05.017.
[36] Herman SD, Mesgarzadeh M, Bonakdarpour A, Dalinka MK. The role of magnetic resonance imaging in giant cell tumor of bone. Skeletal Radiol 1987;16:635–43. https://doi.org/10.1007/bf00357112.
[37] Jha Y, Chaudhary K. Giant cell tumour of bone: a comprehensive review of pathogenesis, diagnosis, and treatment. Cureus 2023;15:e46945. https://doi.org/10.7759/cureus.46945.
[38] Bertrand TE, Cruz A, Binitie O, et al. Do surgical margins affect local recurrence and survival in extremity, nonmetastatic, high-grade osteosarcoma'. Clin Orthop Relat Res 2016;474:677–83. https://doi.org/10.1007/s11999-015-4359-x.
[39] Poitout D, Gaujoux G, Lempidakis M, et al. X-ray computed tomography or MRI in the assessment of bone tumor extension. Chir Memoires l'Acad Chir 1991;117:488–90.
[40] Holland BR, Freyschmidt J. MRI diagnosis of bone tumors. Orthopade 1994;23:355–65.
[41] Ge Q, Xia T, Qiu Y, et al. A semiautomatic segmentation method framework for pelvic bone tumors based on CT-MR multimodal images. Int J Numer Methods Biomed Eng 2023;39:e3697. https://doi.org/10.1002/cnm.3697.
[42] Rich JM, Bhardwaj LN, Shah A, et al. Deep learning image segmentation approaches for malignant bone lesions: a systematic review and meta-analysis. Front Radiol 2023;3:1241651. https://doi.org/10.3389/fradi.2023.1241651.
[43] Sun W, Liu S, Guo J, et al. A CT-based radiomics nomogram for distinguishing between benign and malignant bone tumours. Cancer Imaging 2021;21:20. https://doi.org/10.1186/s40644-021-00387-6.
[44] Copley L, Dormans JP. Benign pediatric bone tumors evaluation and treatment. Pediatr Clin North Am 1996;43:949–66. https://doi.org/10.1016/s0031-3955(05)70444-2.
[45] Restrepo R, Zahrah D, Pelaez L, et al. Update on aneurysmal bone cyst: pathophysiology, histology, imaging and treatment. Pediatr Radiol 2022;52:1601–14. https://doi.org/10.1007/s00247-022-05396-6.
[46] Mahnken A, Nolte-Ernsting C, Wildberger J, et al. Aneurysmal bone cyst: value of MR imaging and conventional radiography. Eur Radiol 2003;13:1118–24. https://doi.org/10.1007/s00330-002-1668-8.
[47] Ladd LM, Roth TD. Computed tomography and magnetic resonance imaging of bone tumors. Semin Roentgenol 2017;52:209–26. https://doi.org/10.1053/j.ro.2017.04.006.
[48] Florkow MC, Willemsen K, Mascarenhas VV, et al. Magnetic resonance imaging versus computed tomography for three-dimensional bone imaging of musculoskeletal pathologies: a review. J Magn Reson Imaging 2022;56:11–34. https://doi.org/10.1002/jmri.28067.
[49] van Timmeren JE, Cester D, Tanadini-Lang S, et al. Radiomics in medical imaging—"how-to" guide and critical reflection. Insights Imaging 2020;11:91. https://doi.org/10.1186/s13244-020-00887-2.
[50] Patiala D of CE (UCoE) Punjabi University, Kaur M, Singh EN. Image segmentation techniques: an overview. IOSR J Comput Eng 2014;16:50–8. https://doi.org/10.9790/0661-16435058.
[51] Zhang R, Lee H, Zhao X, et al. Bone-selective MRI as a nonradiative alternative to CT for craniofacial imaging. Acad Radiol 2020;27:1515–22. https://doi.org/10.1016/j.acra.2020.03.001.
[52] Liu J, Udupa JK, Saha PK, et al. Rigid model-based 3D segmentation of the bones of joints in MR and CT images for motion analysis. Méd Phys 2008;35:3637–49. https://doi.org/10.1118/1.2953567.
[53] Yepes-Calderon F, McComb JG. Eliminating the need for manual segmentation to determine size and volume from MRI. A proof of concept on segmenting the lateral ventricles. PloS One 2023;18:e0285414. https://doi.org/10.1371/journal.pone.0285414.
[54] Chi W, Ma L, Wu J, et al. Deep learning-based medical image segmentation with limited labels. Phys Med Biol 2020;65:235001. https://doi.org/10.1088/1361-6560/abc363.
[55] Kim H, Shin K, Kim H, et al. Can deep learning reduce the time and effort required for manual segmentation in 3D reconstruction of MRI in rotator cuff tears? PloS One 2022;17:e0274075. https://doi.org/10.1371/journal.pone.0274075.
[56] Yang J, Huang S-C. Method for evaluation of different MRI segmentation approaches. IEEE Trans Nucl Sci 1999;46:2259–65. https://doi.org/10.1109/23.819313.
[57] Fenster A, Chiu B. Evaluation of segmentation algorithms for medical imaging. In: 2005 IEEE Eng med biol 27th Annu Conf. 2005; 2005. p. 7186–9. https://doi.org/10.1109/iembs.2005.1616166.
[58] Taha AA, Hanbury A. Metrics for evaluating 3D medical image segmentation: analysis, selection, and tool. BMC Méd Imaging 2015;15:29. https://doi.org/10.1186/s12880-015-0068-x.
[59] Zou KH, Warfield SK, Bharatha A, et al. Statistical validation of image segmentation quality based on a spatial overlap index1 scientific reports. Acad Radiol 2004;11:178–89. https://doi.org/10.1016/s1076-6332(03)00671-8.
[60] Wu P-K, Chen C-F, Chen C-M, et al. Grafting for bone defects after curettage of benign bone tumor – analysis of factors influencing the bone healing. J Chin Méd Assoc 2018;81:643–8. https://doi.org/10.1016/j.jcma.2017.08.024.
[61] Helguero CG, Kao I, Komatsu DE, et al. Improving the accuracy of wide resection of bone tumors and enhancing implant fit: a cadaveric study. J Orthop 2015;12:S188–94. https://doi.org/10.1016/j.jor.2015.10.010.